Self-reconstructing sectioned Bessel beams offer submicron optical sectioning for large fields of view in light-sheet microscopy

Florian O. Fahrbach,[1,2,*] Vasily Gurchenkov,[3] Kevin Alessandri,[3] Pierre Nassoy,[3,4] and Alexander Rohrbach[1,5,6]

[1]*Laboratory for Bio- and Nano-Photonics, Department of Microsystems Engineering, University of Freiburg, Freiburg, Germany*
[2]*Max Planck Institute of Molecular Cell Biology and Biology and Genetics, Dresden, Germany*
[3]*Institut Curie, Centre de Recherche, Paris, F-75248 France*
[4]*LP2N, Institut d'Optique, CNRS UMR 5298 & Université de Bordeaux 1, F-33405 Talence, France*
[5]*Centre for Biological Signalling Studies (bioss), University of Freiburg, Freiburg, Germany*
[6]*rohrbach@imtek.de*
[*]*fahrbach@mpi-cbg.de*

Abstract: One of main challenges in light-sheet microscopy is to design the light-sheet as extended and thin as possible - extended to cover a large field of view, thin to optimize resolution and contrast. However, a decrease of the beam's waist also decreases the illumination beam's depth of field. Here, we introduce a new kind of beam that we call sectioned Bessel beam. These beams can be generated by blocking opposite sections of the beam's angular spectrum. In combination with confocal-line detection the optical sectioning performance of the light-sheet can be decoupled from the depth of field of the illumination beam. By simulations and experiments we demonstrate that these beams exhibit self-reconstruction capabilities and penetration depths into thick scattering media equal to those of conventional Bessel beams. We applied sectioned Bessel beams to illuminate tumor multicellular spheroids and prove the increase in contrast. Sectioned Bessel beams turn out to be highly advantageous for the investigation of large strongly scattering samples in a light-sheet microscope.

OCIS codes: (110.0180) Microscopy; (140.3300) Laser beam shaping; (290.0290) Scattering.

References and links

1. J. Huisken, J. Swoger, F. Del Bene, J. Wittbrodt, and E. H. K. Stelzer, "Optical sectioning deep inside live embryos by Selective Plane Illumination Microscopy," Science **305**(5686), 1007–1009 (2004).
2. H.-U. Dodt, U. Leischner, A. Schierloh, N. Jährling, C. P. Mauch, K. Deininger, J. M. Deussing, M. Eder, W. Zieglgänsberger, and K. Becker, "Ultramicroscopy: three-dimensional visualization of neuronal networks in the whole mouse brain," Nat. Methods **4**(4), 331–336 (2007).
3. P. J. Keller, A. D. Schmidt, J. Wittbrodt, and E. H. K. Stelzer, "Reconstruction of Zebrafish early embryonic development by Scanned Light Sheet Microscopy," Science **322**(5904), 1065–1069 (2008).
4. F. O. Fahrbach and A. Rohrbach, "A line scanned light-sheet microscope with phase shaped self-reconstructing beams," Opt. Express **18**(23), 24229–24244 (2010).
5. F. O. Fahrbach, P. Simon, and A. Rohrbach, "Microscopy with self-reconstructing beams," Nat. Photonics **4**(11), 780–785 (2010).
6. T. A. Planchon, L. Gao, D. E. Milkie, M. W. Davidson, J. A. Galbraith, C. G. Galbraith, and E. Betzig, "Rapid three-dimensional isotropic imaging of living cells using Bessel beam plane illumination," Nat. Methods **8**(5), 417–423 (2011).
7. F. O. Fahrbach and A. Rohrbach, "Propagation stability of self-reconstructing Bessel beams enables contrast-enhanced imaging in thick media," Nat Commun **3**, 632 (2012).
8. L. Silvestri, A. Bria, L. Sacconi, G. Iannello, and F. S. Pavone, "Confocal light sheet microscopy: micron-scale neuroanatomy of the entire mouse brain," Opt. Express **20**(18), 20582–20598 (2012).

#185263 - $15.00 USD Received 12 Feb 2013; revised 8 Apr 2013; accepted 12 Apr 2013; published 2 May 2013

9. E. Baumgart and U. Kubitscheck, "Scanned light sheet microscopy with confocal slit detection," Opt. Express **20**(19), 21805–21814 (2012).
10. J. C. Gutiérrez-Vega, M. D. Iturbe-Castillo, and S. Chávez-Cerda, "Alternative formulation for invariant optical fields: Mathieu beams," Opt. Lett. **25**(20), 1493–1495 (2000).
11. J. C. Gutiérrez-Vega, M. D. Iturbe-Castillo, G. A. Ramirez, E. Tepichín, R. M. Rodríguez-Dagnino, S. Chávez-Cerda, and G. H. C. New, "Experimental demonstration of optical Mathieu beams," Opt. Commun. **195**(1-4), 35–40 (2001).
12. S. Grill and E. H. K. Stelzer, "Method to calculate lateral and axial gain factors of optical setups with a large solid angle," J. Opt. Soc. Am. A **16**(11), 2658–2665 (1999).
13. M. D. Feit and J. A. Fleck, Jr., "Light propagation in graded-index optical fibers," Appl. Opt. **17**(24), 3990–3998 (1978).
14. A. Rohrbach, "Artifacts resulting from imaging in scattering media: a theoretical prediction," Opt. Lett. **34**(19), 3041–3043 (2009).
15. T. Ersoy, B. Yalizay, and S. Akturk, "Self-reconstruction of diffraction-free and accelerating laser beams in scattering media," J. Quantum Spec. Rad. Trans. **113**(18), 2470–2475 (2012).
16. M. Schrader, U. G. Hofmann, and S. W. Hell, "Ultrathin fluorescent layers for monitoring the axial resolution in confocal and two-photon fluorescence microscopy," J. Microsc. **191**(2), 135–140 (1998).
17. G. Vicidomini, M. Schneider, P. Bianchini, S. Krol, T. Szellas, and A. Diaspro, "Characterization of uniform ultrathin layer for z-response measurements in three-dimensional section fluorescence microscopy," J. Microsc. **225**(1), 88–95 (2007).
18. T. V. Truong, W. Supatto, D. S. Koos, J. M. Choi, and S. E. Fraser, "Deep and fast live imaging with two-photon scanned light-sheet microscopy," Nat. Methods **8**(9), 757–760 (2011).

1. Introduction

Light-sheet microscopy provides true optical sectioning by sample illumination with a thin light-sheet. The technique is able to deliver high-contrast images of large samples at high speeds with low photo-damage and bleaching. Conventionally, samples are illuminated by a static light-sheet formed by a strongly elliptical beam from one [1] or two sides [2]. Alternatively, Gaussian beams [3] or Bessel beams [4–6] are laterally scanned in the plane of focus. However, for all illumination techniques presented so far, the thickness of the illuminated volume increases with the size of the image along the illumination optical axis. Therefore, optical sectioning and image contrast decrease for large samples.

Superior contrast and improved resolution were achieved for Bessel beam illumination by employing a confocal-line detection scheme [7]. The principle of confocal-line detection light-sheet microscopy consists in acquiring the image line-wise at the position of the illumination beam while it is scanned across the sample. The method is also able to increase contrast for Gaussian beam illumination [8, 9], if the beams exhibits sufficient propagation stability along a line.

Here, we introduce a new kind of beam that we call sectioned Bessel beam (SBB) that can be generated by blocking opposite sections of the beam's angular spectrum. Sectioned Bessel beams are similar to Mathieu beams, a solution to the Helmholtz-equation in parabolic coordinates. But even though Mathieu beams have been investigated for a long time [10, 11], no study on their propagation performance in strongly scattering media has been reported so far. First, we give analytical descriptions for shape and dimensions of the SBB. We further present results from computer simulations with the Beam Propagation Method (BPM) and analyze the penetration depth into scattering media. Using simulation data, we demonstrate in section 6 the influence of the section angle of the SBB's angular spectrum on the optical sectioning capability of the light-sheet. Moreover, we show that SBBs in combination with confocal-line detection allows to decouple the optical sectioning from the depth of the field of the illumination beam and thereby the object size. Finally, we analyze the performance of SBBs in strongly scattering tumor multicellular spheroids with regard to penetration depth and image contrast.

2. Sectioned Bessel beams - shapes and dimensions

A typical (zero-order) Bessel beam used in light-sheet microscopy is characterized by its angular spectrum $\tilde{E}_B$, which consists of a thin ring of finite thickness. It can be described

#185263 - $15.00 USD Received 12 Feb 2013; revised 8 Apr 2013; accepted 12 Apr 2013; published 2 May 2013

by $\tilde{E}_B(k_x,k_y) = \tilde{E}_0\left(\Theta(k_0\mathrm{NA}_B - k_r) - \Theta(\sqrt{\varepsilon}\,k_0\mathrm{NA}_B - k_r)\right)$ with $k_r = \left(k_x^2 + k_y^2\right)^{1/2}$. Here Θ(k) denotes the Heaviside step function and $\mathrm{NA}_B = n\cdot\sin\alpha$ describes the maximum focusing angle of the Bessel beam. ε < 1 is the ring width parameter, i.e. the area ratio of the inner to the outer disc [4]. The outer radius of the annular spectrum is $k_0\mathrm{NA}_B$, the ring thickness is $k_0\mathrm{NA}\cdot(1-\sqrt{\varepsilon})$. For ε = 0, the back aperture is homogeneously illuminated and a conventional beam with a limited depth of field $dz = \lambda/(n - n\cos\alpha)$ is created.

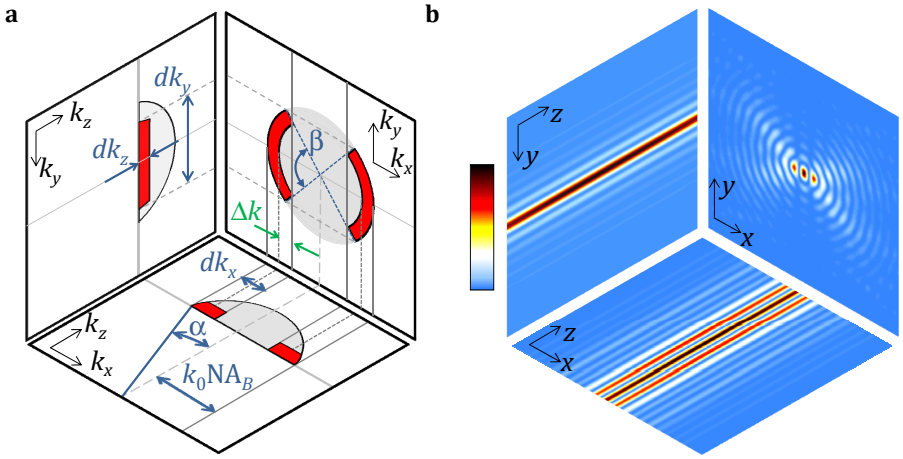

Fig. 1. A sectioned Bessel beam in k-space and in real space. **(a)** The extents dk_x, dk_y, dk_z, of the sectioned angular spectrum (red areas) as a projection of the Ewald spherical cap define the dimensions of the beam. **(b)** The intensity cross-sections $I(x,y,z = 0)$, $I(x,y = 0,z)$ and $I(x = 0,y,z)$ illustrate the section angle β, but also show the propagation invariance.

Other than Bessel beams with a complete ring-shaped angular spectrum, the spectrum of a sectioned Bessel beam consists of two opposed sections of the ring - each spanning over an angle β as pointed out in Fig. 1(a) in the k_xk_y-plane. The red-shaded areas are projections of the Ewald-sphere onto the three orthogonal planes in k-space. In the k_xk_y-plane the angular spectrum representation $\tilde{E}(k_x,k_y)$ exhibits a point symmetry with respect to the optical z-axis. Mathematically, the spectrum can be sufficiently well described by

$$\tilde{E}_{\mathrm{SeB}}(k_x,k_y) = \tilde{E}_0\left(\Theta(k_0\mathrm{NA}_\mathrm{B} - k_r) - \Theta(\sqrt{\varepsilon}\,k_0\mathrm{NA}_\mathrm{B} - k_r)\right)\cdot\mathrm{rect}\left(\frac{k_y}{2k_0\mathrm{NA}_\mathrm{B}\cdot\sin(\beta/2)}\right) \quad (1)$$

where β is the angular width and rect is defined as rect(x/b) = 1 if $|x| \le b/2$ and 0 otherwise. β = 180° results in a conventional Bessel ring spectrum, since the rect-function does not cut-off any frequencies.

Correspondingly, the field of a Bessel beam in real space can be obtained by an inverse Fourier transform:

$$E_{\mathrm{SeB}}(x,y,z) = \frac{A}{r}\left(J_1(k_0\mathrm{NA}_\mathrm{B}\,r) - \sqrt{\varepsilon}J_1\left(\sqrt{\varepsilon}\,k_0\mathrm{NA}_\mathrm{B}\,r\right)\right) * \mathrm{sinc}\left(k_0\mathrm{NA}_\mathrm{B}\cdot\sin(\beta/2)\cdot y\right) \quad (2)$$

where $r = \sqrt{x^2+y^2+z^2}$ is the distance to the beam center, $A = \left(2\pi^2 k_0\mathrm{NA}(\varepsilon-1)\right)^{-1}$ is a factor and the symbol (*) denotes the convolution operation. The intensity cross-sections $|E_{\mathrm{SeB}}(x,y)|^2$, $|E_{\mathrm{SeB}}(x,z)|^2$ and $|E_{\mathrm{SeB}}(y,z)|^2$ are shown in Fig. 1(b). Here and throughout this study x is the beam scanning direction parallel to the light-sheet, y is the direction of the detection optical axis perpendicular to the light-sheet.

#185263 - $15.00 USD Received 12 Feb 2013; revised 8 Apr 2013; accepted 12 Apr 2013; published 2 May 2013

It can be seen that the Bessel rings are suppressed in the detection *y*-direction because of the convolution with the sinc-function, which has a slightly different frequency than the J_1-functions (Eq. (2)) along *y*. This has important implications for the application in light-sheet microscopy as will be shown below.

From Eq. (1) and by inspecting the corresponding Fig. 1(a), it is straight forward to estimate the dimensions of the main lobe of the sectioned Bessel beam. These are defined by the inverse of the extents dk_x, dk_y and dk_z, as projections of the spectrum $\tilde{E}_{\mathrm{SeB}}(k_x, k_y, k_z)$ onto the axes and can be described by the adjustable parameters ε, β and $\mathrm{NA_B}$. The outer-diameter of the ring-spectrum is $2k_0 \cdot \mathrm{NA_B}$ and is defined by the NA of the focusing lens, $\mathrm{NA_B}$. The inner diameter is $2\sqrt{\varepsilon} \cdot k_0 \cdot \mathrm{NA_B}$. The extent of the angular spectrum $\tilde{E}_{\mathrm{SeB}}(k_x, k_y)$ in k_y-direction is solely determined by the section's angular extent, β, such that $dk_y = 2k_0 \cdot \mathrm{NA}_B \cdot \sin(\beta/2)$, i.e. the width of the rect-function. The ring thickness determines the axial extent of the spectrum dk_z, which scales with the ring parameter ε such that $dk_z = k_0 \cdot (\cos\alpha - \varepsilon \cdot \cos\alpha) \approx 2k_0 \cdot \mathrm{NA}_B^2 \cdot (1-\varepsilon)$ in the paraxial approximation.

As shown in Fig. 1(a) the spectrum in k_x-direction consists of two fragments of width dk_x in an outer distance of $\Delta k_x = 2k_0 \cdot \mathrm{NA_B}$ to each other. The frequency Δk_x defines the radial ring spacing of a Bessel beam. After projection in the pupil plane (angular spectrum), the (red) ring area on the Ewald sphere consists of the ring thickness $(1-\sqrt{\varepsilon})$ and the $(1-\cos(\beta/2))$ part (see distance Δk indicated in green in Fig. 1(a)), such that $dk_x = k_0 \cdot \mathrm{NA}_B \cdot (1-\sqrt{\varepsilon}) + \sqrt{\varepsilon} \cdot k_0 \cdot \mathrm{NA}_B \cdot (1-\cos(\beta/2)) = k_0 \cdot \mathrm{NA}_B \cdot (1-\sqrt{\varepsilon} \cdot \cos(\beta/2))$. dk_x defines the width of the beam envelope of the sectioned Bessel beam in scan direction as shown in Fig. 1(b).

From the uncertainty relation $dj \cdot dk_j = 2\pi$ ($j = x,y,z$) we obtain the following extents of a sectioned Bessel beam with section angle β:

$$dx = \frac{\lambda}{\mathrm{NA}_B \cdot \left(1 - \sqrt{\varepsilon}\cos(\beta/2)\right)} \tag{3a}$$

$$dy = \frac{\lambda}{\mathrm{NA}_B \cdot \sin(\beta/2)} \tag{3b}$$

$$dz = \frac{4 \cdot \lambda \cdot n}{\mathrm{NA}_B^2 \cdot (1-\varepsilon)} \tag{3c}$$

These beam extents *dx*, *dy* and *dz* represent effective widths and correspond to real space standard deviations obtained by the inverse of the standard deviations in *k*-space [12]. The full width (root distance) *dx* in scan direction describes the envelope of the modulated beam, but does not describe a Bessel beam with $\beta = 180°$. Whereas *dz* is independent of β, the dependency of the beam widths *dx* and *dy* on the section angle β is displayed in Fig. 2(a) (with $\varepsilon = 0.8$ and $\mathrm{NA_B} = 0.4$). It can be seen that $dx(\beta)$ and $dy(\beta)$ become minimal for β approaching 180°, which corresponds to a conventional Bessel beam with finite ring width. However, for a reasonable range of section angles $\beta > 60°$, it turns out that the width *dy* in detection direction hardly changes with β, whereas *dx* falls of strongly. In other words, the light sheet thickness *dy* is nearly independent of β for $\beta > 60°$.

#185263 - $15.00 USD Received 12 Feb 2013; revised 8 Apr 2013; accepted 12 Apr 2013; published 2 May 2013

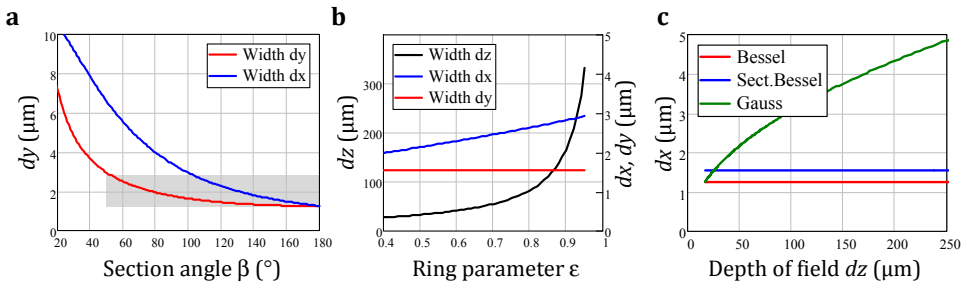

Fig. 2. Change of the effective beam widths. **(a)** The lateral beams widths of a sectioned Bessel beam change slowly along the detection axis *y*, but fall off strongly in beam scanning *x*-direction for angles β > 50°. **(b)** The depth of field *dz* can be controlled by the ring thickness ε, which has only a minor effect on the lateral width *dx* and no effect on *dy*. The curves shown are for β = 0.6π~110°. **(c)** The width *dy* of the Gaussian beam increases with increasing depth of field *dz*, which is not the case for both types of Bessel beams according to the angular spectrum estimation.

As shown in Fig. 2(b), a Bessel beam's depth of field *dz* can be steered efficiently by varying the ring parameter ε = 0.7…0.95. This has a small effect on the lateral width *dx* and no effect on *dy*. By plotting *dy*(NA) against *dz*(NA) for the Gaussian beam (ε = 0 and β = 180°) as shown in Fig. 2(c), one finds that for a decreasing NA or increasing depth of field *dz*(NA) the width *dy*(NA) increases. For the conventional Bessel beam (β = 180°) and the sectioned Bessel beam (β = 100°), the widths *dy*(ε) remain constant when increasing *dz*(ε) via the ring parameter ε. As we will show below, this situation changes when the detection point-spread function $PSF_{det}(x,y,z)$ is considered.

Note that these measures do not account for the total fluorescence excited by the beams. These beam extents do not represent the optical sectioning capability, i.e. how well the beams are suited in order to detect fluorescence only from a thin region around the focal plane of the detection objective lens. Data on the optical sectioning performance will be shown in sections 5 & 6.

3. Measures for directional propagation stability

So far, only beam widths for free-space propagation have been considered. Analysis of the propagation behavior of sectioned Bessel beams in inhomogeneous media yields a quantitative measure for their self-reconstruction ability. First, we pursued a numerical beam propagation approach.

In the following, a measure for directional propagation stability is introduced. To assess how strongly the beams are scattered or deflected by obstacles, we measure the power that the beam carries up to a certain radius around its propagation axis:

$$P(z;R) = \int_{x^2+y^2<R^2} I(x,y,z)\,dxdy. \tag{4}$$

where $I(x,y,z) = |E_{SeB}(x,y,z) + E_{sca}(x,y,z)|^2$ is the interference of the unscattered field E_{SeB} (Eq. (1)) and the manifold scattered field E_{sca}. By normalizing the power of the beam propagating through a scattering sample P_{scat} to the power P_{ideal} of the corresponding unscattered beam one obtains

$$Q(z;R) = \frac{P_{scat}(z;R)}{P_{ideal}(z;R)} \tag{5}$$

Q gives the relative power that a beam is able to maintain within a small radius *R* around its axis in the presence of scatterers. *Q* It is robust against natural beam spreading due to

#185263 - $15.00 USD Received 12 Feb 2013; revised 8 Apr 2013; accepted 12 Apr 2013; published 2 May 2013

diffraction in homogeneous space and comparable for beams which differ in irradiance and total power. The power ratio averaged over Δz along the propagation axis

$$\overline{Q}(R) = \frac{1}{\Delta z} \int_{\Delta z} Q(z;R)dz \tag{6}$$

allows to assess the beam's propagation stability with a single number – which means a reduction in data of $>10^7$:1 in comparison to the full volume data.

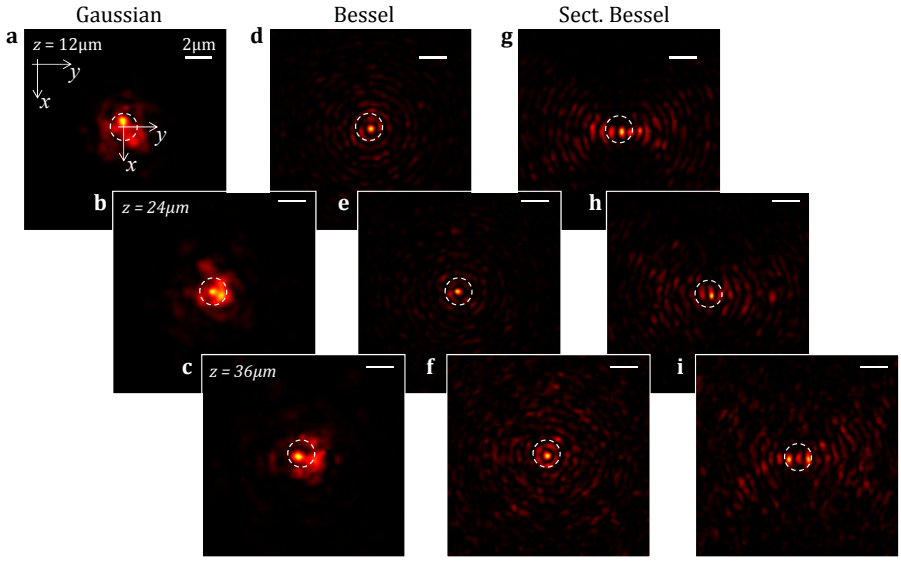

Fig. 3. Simulated intensity cross-sections of a Gaussian and a Bessel beam propagating through a scattering medium. Transverse intensity cross-sections $I(x,y,z = z_i)$ are shown for three different penetration depths z_0 = 12µm, z_1 = 24µm, z_2 = 36µm into a scattering medium for a Gaussian (a), a Bessel beam (b) and a sectioned Bessel beam (c). The medium consists of spheres with d = 2µm, n = 1.41 at a volume concentration of ρ = 6\%. Integration over the area around the beam's propagation axis yields the beam's on axis power $P(z,R$ = 2µm). The region is marked by a dashed circle.

A measure for directional propagation stability can be used to answer the following question: Does the beam follow its initial direction even in the presence of phase perturbations induced by scatterers? Or, put in a more quantitative way: How much energy is taken out of the beam's central region (radius R) relative to the ideal, unscattered beam as a function of propagation distance z? This measure is relevant to microscopy: Good images with homogeneous illumination require that this power is independent of the perturbation of the beam. The change of the beam's on-axis power at different positions in a sample that arises from different scattering of the beam is a major source of image artifacts. Its strength can be measured by the standard deviation of the position dependence of the on-axis power [5].

4. Simulation results for directional propagation stability

At first, we numerically investigated the propagation of coherent beams through scattering samples using the Beam Propagation Method (BPM) [13, 14]. The standard Gaussian beam focused by NA = 0.08 is compared to two Bessel beams: one with a low NA (NA = 0.2, ε = 0.74) and one with a high NA (NA = 0.4, ε = 0.94). Additionally, a sectioned Bessel beam with a high NA (NA = 0.4, ε = 0.94) and an azimuthal width of the section of β = 88° was analyzed. All beams exhibit equal depth of field of dz≈100µm. Cross-sections of the beams are shown in Fig. 3.

#185263 - $15.00 USD Received 12 Feb 2013; revised 8 Apr 2013; accepted 12 Apr 2013; published 2 May 2013

The scattering medium is represented by a distribution of silica spheres with refractive index of n_{scat} = 1.41 embedded in an aqueous gel with n_{med} = 1.33. A small imaginary refractive index (n_i = 0.0004) is included to account for the beam energy that is lost due to backscattered light, which the BPM cannot account for otherwise. The simulations were performed for different parameters of the scattering sample, i.e. volume concentrations (ρ = 6%, ρ = 12%) and size (d = 2µm, d = 4µm). To obtain representative results, the beams were propagated at 9 different (x_i, y_i) positions for 15 different arrangements of the spheres expressed by $n_j(x,y,z)$. The stability ratio $\overline{Q}(z)$ was then computed as the average over all 9 beam positions in all 15 samples.

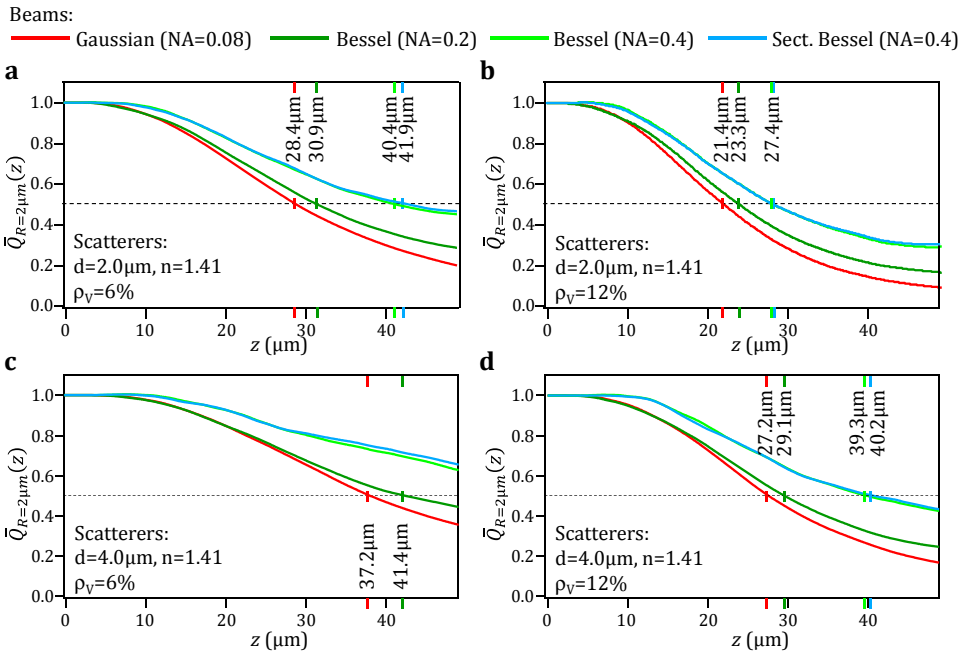

Fig. 4. On-axis power for different illumination beams propagating through scattering media. The graphs show the on-axis power $\overline{Q}(z; R = 2\mu m)$ for different beams. The shown data was averaged over 9 beam positions in 15 different scattering media and normalized to equal values at z = 0µm. The scattering medium consists of randomly distributed spheres with a difference in refractive index of Δn = 0.08 with respect to the surrounding volume. The diameter of the spheres is d = 2.0µm in (a), (b) and d = 4.0µm in (c), (d). The volume concentration is ρ_V = 6% in (a), (c) and ρ_V = 12% in (b), (d).

The results are shown in Fig. 4. It can be seen that $\overline{Q}(z)$ is similar for the Gaussian beam and the low-NA Bessel beam. For both beams the values of $\overline{Q}(z)$ for large z are inferior to those for the high-NA Bessel beam and surprisingly also the sectioned Bessel beam with a high NA. This result means that the relative power of the beam within a radius R around the propagation axis is higher for (sectioned) Bessel beams if the NA of the beam is high. The penetration depth is higher for larger spheres for all illumination beams. These obstacles scatter more light in forward direction, i.e. they remove less light from the beams. This result qualitatively agrees with a rough estimate using the reduced scattering coefficient $\mu'_{scat} = (1-g)\cdot\mu_{scat}$ where g is the size-dependent scattering anisotropy factor (for λ = 488nm: $g_{2\mu m}$ = 0.96, $g_{4\mu m}$ = 0.99).

The data obtained was analyzed in more detail. Figure 5 shows the average power ratio along the simulated volume according to Eq. (6) in dependence of the beam position i (lateral

#185263 - $15.00 USD Received 12 Feb 2013; revised 8 Apr 2013; accepted 12 Apr 2013; published 2 May 2013

axis) and the volume j (vertical axis). The magnitude of $\overline{Q}_{i,j}$ is coded by the color of the spot for each of the beam positions i = 1...9 in each of the volumes j = 1...15 corresponding to 135 simulations for each beam type. While white represents $\overline{Q}_{i,j}$ = 1, meaning that the power is approximately equal in the scattered and unscattered case, green and blue spots indicate weak intensity and a low power of the beam in the area around the propagation axis. Note that the relative on-axis power decreases monotonously, which is a prerequisite for the conclusions drawn from the values of $\overline{Q}_{i,j}$. A large difference between the results for a Gaussian beam and the various Bessel beams can be observed. The variance of the values $\overline{Q}_{i,j}$ is high for the Gaussian beam while it is small for the Bessel beam. This finding indicates the stronger susceptibility of the Gaussian beam to beam deflections and scattering.

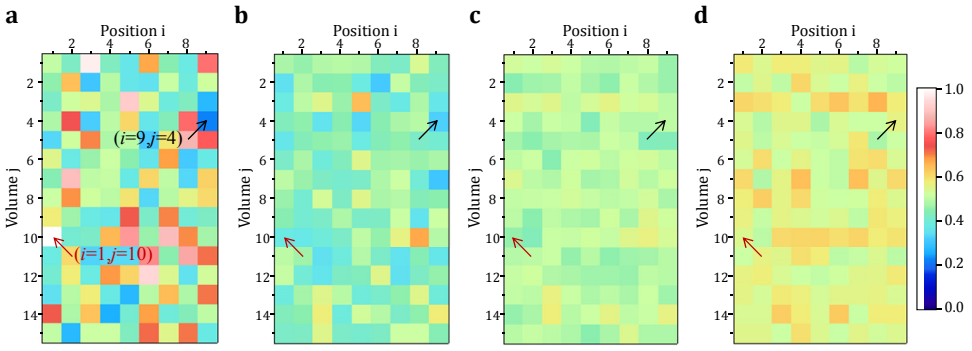

Fig. 5. Average normalized on-axis power for beams propagating through distributions of scattering spheres at different beam positions. The average on-axis power $\overline{Q}_{i,j}$ for beams that propagate through a scattering medium consisting of spheres (d = 2µm, Δn = 0.08, ρ_V = 6%) is shown for different beam positions i and different random position configurations of the spheres j. The color codes the on-axis power average along the propagation distance through the scattering spheres for: **(a)** a Gaussian beam with NA = 0.08, **(b)** a Bessel beam with a low NA = 0.2, **(c)** a Bessel beam with a high NA = 0.4, and **(d)** a sectioned Bessel beam with the same NA and β = 88°. The variation in the values $\overline{Q}_{i,j}$ is strongest for the Gaussian beam and weakest for the high-NA Bessel beam and sectioned Bessel beam.

It is interesting to inspect the intensity distribution of the beams for two extreme situations, i.e. position i = 1 in volume j = 10 where $\overline{Q}_{i,j}$ is exceptionally high for the Gaussian beam and position i = 9 in volume j = 4 where $\overline{Q}_{i,j}$ for the Gaussian beam is very low (marked by arrows in Fig. 5). In the first case, the Gaussian beam propagates through a region practically without spheres and therefore remains almost unperturbed, whereas in the second case obstacles close to the beam axis perturb the beam strongly and deflect it from its initial propagation direction. In contrast, the Bessel beam and the sectioned Bessel beam generated at a high NA = 0.4 exhibit a very weak perturbation in both cases that mainly affects the ring system. Most importantly, the main lobe is neither deflected nor strongly distorted. It can be seen in Fig. 3 that for i = 1 & j = 4, i.e. an average value of $\overline{Q}_{i,j}$, the central peak of both beams is quite well maintained of the whole distance. The main lobe of the Bessel beam is much more confined and is well separated from the ring system, whereas the Gaussian beam is blurred over a larger area.

From the simulation results shown in Figs. 4 and 5 the following conclusions can be drawn. Gaussian beams show penetration depths and directional propagation stabilities that are inferior to those of high-NA Bessel beams, but not to those of low-NA Bessel beams. Remarkably, high-NA sectioned Bessel beams are equally robust against scattering as Bessel beams with the same NA. Moreover, Gaussian beams are much more sensitive to local perturbations by scatterers so that the average on-axis intensity is more position dependent.

#185263 - $15.00 USD Received 12 Feb 2013; revised 8 Apr 2013; accepted 12 Apr 2013; published 2 May 2013

This difference between Gaussian and Bessel beam is partly due to the larger cross-section of the Bessel beams: more scatterers affect the beam, but the impact of each single scatterer is much lower.

5. Theoretical considerations on optical sectioning

The profile of a sectioned Bessel beam is characterized by the fact that the central lobe of the beam is mainly fed by self-healing photons from the sides along the scan axis x. If sectioned Bessel beams are used to illuminate a thin line and fluorescence along this line is detected using the confocal-line detection scheme [7] it is expected that less background will be recorded. This kind of beam-engineering bares an interesting application potential and will be investigated in detail in the following.

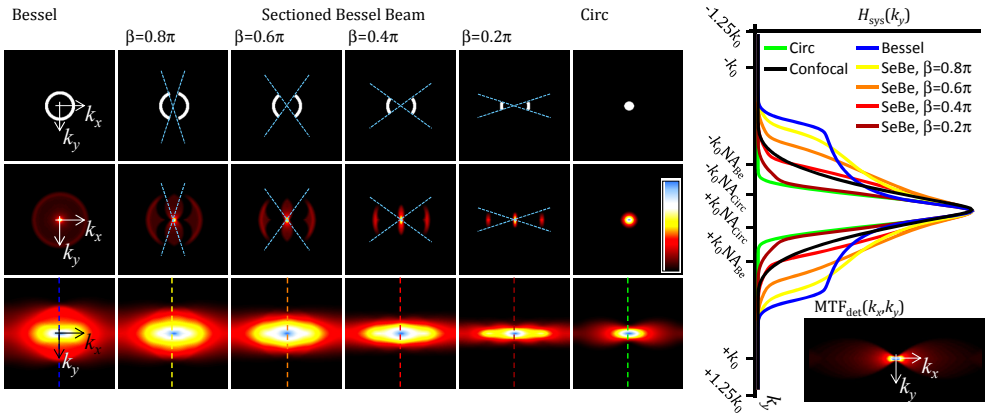

Fig. 6. Transfer functions of fields and intensities for (sectioned) Bessel beams and a conventional (flat-top) beam. The table shows the coherent transfer functions $\tilde{E}(k_x,k_y)$ (angular spectrum) in the upper rows, the intensity transfer functions $AC(\tilde{E})$ in the second row, and the system transfer function $H_{sys}(k_x,k_y)$ in the bottom row. The red and yellow areas in $H_{sys}(k_x,k_y)$ give an estimate for the ratio of high-frequency and medium frequency information of the beam. Vertical line scans $H_{sys}(k_y)$ along the detection axis are plotted on the right and reveal the ratios of high- and low-frequency contributions. The detection $MTF_{det}(k_x,k_y)$ is shown as an inset (bottom right).

The confocal system point-spread function can be assumed to be a product of intensities:

$$h_{sys}(x,y) = h_{ill}(x,y) \cdot h_{det}(x,y) \tag{7}$$

Following [7] an image p_{CL} obtained by confocal-line detection (CL) from a fluorophore distribution $c_F(\mathbf{r})$ can be approximated by

$$p_{CL}(\mathbf{r}) = \left[h_{ill}(\mathbf{r}) \cdot h_{det}(\mathbf{r})\right] * c_F(\mathbf{r}) \tag{8}$$

where the symbol '*' designates a convolution. In Fourier space Eq. (8) is the convolution of the corresponding transfer functions:

$$H_{sys}(\mathbf{k}) = H_{ill}(\mathbf{k}) * H_{det}(\mathbf{k}) = AC\left\{\tilde{E}_{ill}(\mathbf{k})\right\} * AC\left\{\tilde{E}_{det}(\mathbf{k})\right\} \tag{9}$$

where $\tilde{E}_{ill}(\mathbf{k})$ and $\tilde{E}_{det}(\mathbf{k})$ are the Fourier transforms of the illuminating field (Eq. (2)) and of the coherent detection PSF. AC{..} designates the auto-correlation.

Figure 6 displays the confocal transfer function $H_{sys}(\mathbf{k},\beta)$ for various section angles. The first row illustrates projections of the angular spectrum $\tilde{E}_{ill}(k_x,k_y,\beta)$ along the beam propagation axis z. The second row shows $H_{ill}(k_x,k_y,\beta) = AC[\tilde{E}_{ill}(k_x,k_y,\beta)]$, whereas $H_{sys}(k_x,k_y,\beta)$ is shown in the third row. From the shape of $H_{sys}(k_x,k_y,\beta)$, the beam's sectioning capability can

#185263 - $15.00 USD Received 12 Feb 2013; revised 8 Apr 2013; accepted 12 Apr 2013; published 2 May 2013

be estimated. It is roughly expressed by the ratio of high spatial frequencies (HSF) to medium/low high spatial frequencies (LSF) of the MTF. The LSF components lie close to the center of the axis which appears in yellow and white for all beams indicating the largest amplitudes. Medium amplitudes are shown in red and extend to the highest frequencies (i.e. largest distances to the center) for the conventional Bessel beam. The line-profiles shown to the right of Fig. 6 confirm that the Bessel beam MTF contains the highest spatial frequencies. However, the support for medium frequencies (see extent of yellow areas in $H_{sys}(k_x,k_y)$) is smaller in comparison to the sectioned Bessel beam for $\beta = 0.6\ldots 0\ 8\pi$. This finding indicates the different sectioning capability for sectioned Bessel beams as analyzed in detail below.

The system's point-spread function $h_{sys}(\mathbf{r})$ (see Eq. (7)), can be measured in 3D when $c_F(\mathbf{r})$ corresponds to a small fluorescent sphere. The integral over $h_{sys}(\mathbf{r})$ is a measure for the total fluorescence signal. To quantify the optical sectioning performance we compute the total fluorescence as a function of the detection axis, such that

$$F(y) = \iint h_{sys}(x,y,z)\,\mathrm{d}x\mathrm{d}z = \iint H_{sys}(k_x,y,k_z)\,\mathrm{d}k_x\mathrm{d}k_z. \tag{10}$$

The latter equality results from Parseval's theorem, where $H_{sys}(k_x,k_z)$ is the modulus transfer function of $h_{sys}(x,z)$. The normalized integral of $F(y)$,

$$G(y) = \frac{1}{F_{tot}} \int_{-\infty}^{y} F(y')dy', \tag{11}$$

corresponds to the fluorescence-sea method [16, 17]. The thickness dy_{OS} of the optical section is defined such that

$$G(dy_{OS}/2) - G(-dy_{OS}/2) = 63\% \tag{12}$$

and gives the range along the detection axis out of which the majority of the fluorescence is collected. Alternatively, it is useful to investigate the signal-to background ratio SBG. Here the signal $S = \int_{-\delta}^{\delta} F(y)\mathrm{d}y$ is defined as the fluorescence generated within the depth of field of the detection lens $2\delta \approx 2\lambda / (n\text{-}n\cdot\cos\alpha)$ and the background is the remaining fluorescence. Accordingly, the signal-to-background is

$$\mathrm{SBG} = \int_{-\delta}^{\delta} F(y)\mathrm{d}y \Big/ \left(\int_{\infty}^{-\delta} F(y)\mathrm{d}y + \int_{\delta}^{\infty} F(y)\mathrm{d}y \right) = \frac{G(\delta) - G(-\delta)}{G(-\delta) + (1 - G(-\delta))}. \tag{13}$$

which simplifies to $\mathrm{SBG} = (0.5 - G(-\delta)) / G(-\delta)$ for $F(y) = F(-y)$.

6. Influence of the section angle β on optical sectioning

For optimum image quality we seek the angle β that provides the best optical sectioning. Therefore we evaluate the section thickness dy_{OS} for a series of angles β using numerically computed distributions of $h_{sys}(x,y,z)$. The simulation was performed using a discretization of 23nm in a cube with a side length of 4096 pixels (≈94μm). The wavelength λ_0 = 488nm corresponds to 8 pixels in a medium with n = 1.33. Examples for the cross-sections $h_{ill}(x,y)$ of a sectioned Bessel beam for β = 20° and β = 110° and a conventional Bessel beam are shown in Figs. 7(a)-7(c). The ring parameter is ε = 0.9 so that the depth of field is $dz_{1/e}$ ≈80μm. The detection point-spread function is shown in Fig. 7(d).

#185263 - $15.00 USD Received 12 Feb 2013; revised 8 Apr 2013; accepted 12 Apr 2013; published 2 May 2013

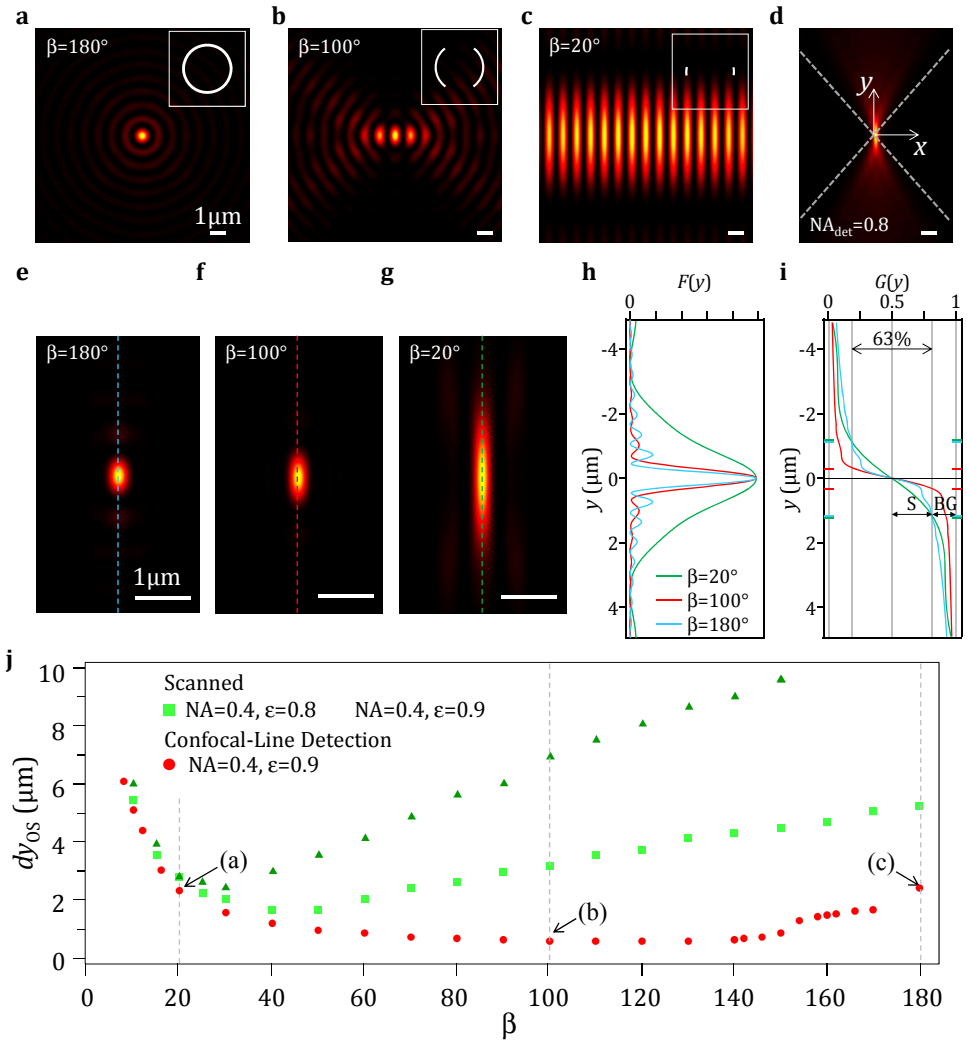

Fig. 7. Optical sectioning performance in light-sheet microscope with sectioned Bessel beam illumination for various section angles. **(a-c)** The simulated cross-section of three sectioned Bessel beams for β = 180°, β = 100°, and β = 20°, respectively. Small insets in the upper left corner illustrate the beams' angular spectrum $\tilde{E}(k_x,k_y)$. **(d)** The *z*-projection of the detection PSF for NA = 0.8. **(e-g)** The system-PSFs are shown below the corresponding illumination beams. **(h)** The fluorescence contribution to the total detected signal from each layer $F(y)$ is shown in **(i)** The normalized primitive of F(y), $G(y)$, where the signal (S) and background (BG) according to Eq. (13) are marked by arrows. **(j)** The optical sectioning dy_{OS} as a function of the section angle β for wide-field detection (green) with different depths of field $dz_{1/e}$ = 40µm and $dz_{1/e}$ = 80µm for ε = 0.8 and ε = 0.9, respectively and for confocal-line detection (red).

First, we analyze optical sectioning dy_{OS} for scanned illumination beams and wide-field detection in a light-sheet microscope. In this case, dy_{OS} depends only on the thickness of the light-sheet. The intensity of the light-sheet is constant along the scan axis (h_{LS} (y,z) ∝ $\int h_{ill}(x,y,z)dx$) and within the depth of field of the beam ($h_{LS}(x,y,z) \approx h_{LS}(y)$), so that one can write $F(y) = \iint h_{LS}(y) \cdot h_{det}(x,y,z)\,dxdz = h_{LS}(y) \cdot \iint h_{det}(x,y,z)\,dxdz$. As the detection lens collects equal amounts of light from each plane, i.e. $\iint h_{det}(x,y,z)\,dxdz$=const, the proportionality $F(y)$ ∝ $h_{LS}(y)$ holds. The section thickness $dy_{OS}(\beta)$ is shown in Fig. 7(j). With NA = 0.4 and

#185263 - $15.00 USD Received 12 Feb 2013; revised 8 Apr 2013; accepted 12 Apr 2013; published 2 May 2013

ε = 0.9, a minimum thickness of dy_{OS} ≈2.5µm is achieved for β = 30° and increases significantly for larger values. At the same NA, thinner light-sheets can only be generated by shorter beams having a smaller ε. For e.g. ε = 0.8 and a Bessel beam with $dz_{1/e}$ ≈40µm, $dy_{1/e}$ ≈1.7µm is possible for β = 50°.

However, there is a fundamental difference in the case of confocal-line detection. As indicated by Fig. 7(d), the detection objective lens collects light from a region that can be roughly approximated as a double cone with opening angle $\alpha_{det} = \sin(NA_{det}/n)$. As described by Eqs. (7) and (10), the optical sectioning depends on the overlap between the illumination beam and the point-spread-function of the detection objective lens. This overlap can be steered for sectioned Bessel beams by adapting the value β relative to α_{det}. The system-point-spread functions h_{sys} corresponding to the beams shown in Figs. 7(a)-7(c) are displayed below in Figs. 7(e)-7(g) for a detection PSF with NA = 0.8 (Fig. 7(d)). It can be seen, that the small value of β = 20° results in a grating-like structure that is only poorly confined along *y*. Accordingly, *F*(*y*), shown in Fig. 7(h) is very broad. For the conventional Bessel beam (Fig. 7(e)), even though the main signal is confined well, the ring structure leads to strong sidelobes of *F*(*y*). The best result, i.e. a small extent of h_{sys} along the *y*-axis (Fig. 7(h)) and weak side-lobes is obtained for the sectioned Bessel beam with β = 100° (Fig. 7(f)). *G*(*y*) is plotted in Fig. 7(i) and exhibits the steepest and narrowest step for the sectioned Bessel beam. Figure 7(j) shows the optical sectioning dy_{OS} for various angles β = 0…180°. The thinnest sections are obtained for angles β in the range of 80° to 140°. Therefore, the optical sectioning for equal depth of field (ε = 0.9) is improved by a factor of ≈4 from dy_{OS} = 2.4µm to dy_{OS} = 0.6µm relative to conventional Bessel beams with confocal-line detection or sectioned Bessel beams with wide-field detection.

7. Optical sectioning dependency on the depth of field

The special angular spectrum of the sectioned Bessel beam cannot only be exploited to improve the optical sectioning, but also to make it independent on the depth of field, i.e. the size of the field of view along the illumination axis. This ability of the sectioned Bessel beam stands in sharp contrast to other illumination beams like Gaussian and Bessel beams, where the symmetrical cross-section increase for larger depths of field.

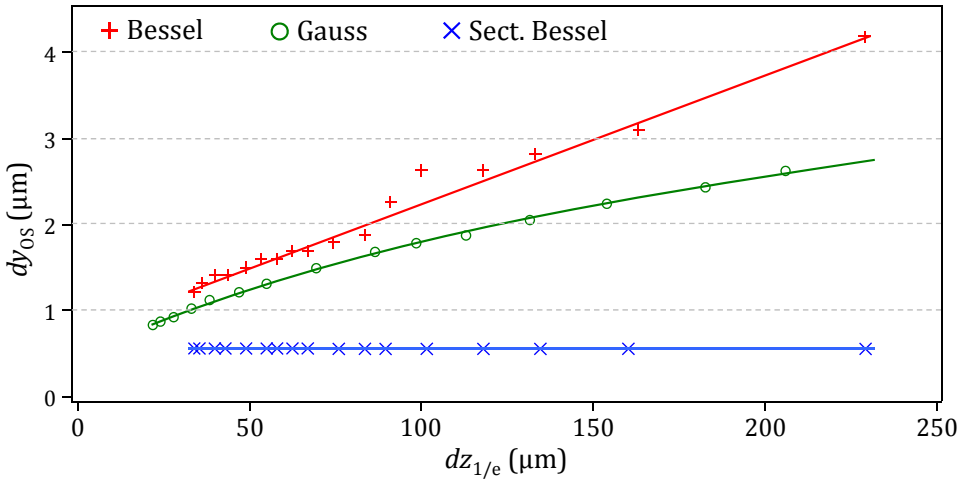

Fig. 8. Optical Sectioning dependency on the depth of field of the illumination beam with confocal-line detection (simulation). The depth of field $dz_{1/e}$ is steered by the NA for the Gaussian beam. For the Bessel beam and the sectioned Bessel beam (β = 110°) with NA = 0.4 the ring parameter ε is adapted.

#185263 - $15.00 USD Received 12 Feb 2013; revised 8 Apr 2013; accepted 12 Apr 2013; published 2 May 2013

In Fig. 8 the optical sectioning for confocal-line detection is plotted against the illumination beam's depth of field for Gaussian, Bessel and sectioned Bessel beams. For the Gaussian beam a nonlinear dependency can be observed that is in agreement with Eq. (3c) predicting a square-root dependence between the Gaussian beam's depth of field Δy and its waist diameter Δz (Fig. 2(c)). Optical sectioning provided by a Bessel beam increases linearly, as can be seen by the good agreement of the values with a fitted line. The steps in the $dy_{OS}(dz)$ originate from the Bessel beam's rings. In contrast, optical sectioning for the sectioned Bessel beams is completely independent on the depth of field. The sectioned Bessel beam's cross-section mainly increases on the sides (along the x-axis) where no light is collected by the detection lens, i.e. the only overlap between the illumination PSF h_{ill} and the detection PSF h_{det} is in the thin beam center around the beam's axis.

8. Images of tumor multicellular spheroids

In addition to the analytical concepts and numerical simulations shown above, experimental results obtained from the imaging of cancer cell clusters are presented in this section. To test the performance of sectioned Bessel beams we acquired 3D stacks of Tumor Multicellular Spheroids. These Mouse colon carcinoma CT26 spheroids were prepared using a microfluidics-assisted extrusion device (Alessandri et al, to be published) and cultured during 4 days. They were fixed in 4% paraformaldehyde in phosphate buffered saline (PBS) during 1 h at room temperature and incubated with 0.5µg/ml Phalloidin conjugated with Alexa488 (Molecular Probes) in PBS with 1% v/v Triton-X100 (Sigma) at 4°C overnight. The spheroids of about 250µm diameter were mounted in 1% low melting point agarose (Invitrogen) in PBS.

We compare the performance of sectioned Bessel beam illumination combined with confocal-line detection with 3 other imaging modes: scanned Gaussian beam illumination as well as confocal-line detection with Gaussian beams and conventional Bessel beams. For each mode, a stack of 13 images with a spacing of 10µm was recorded. Figures 9(a)-9(d) show images $p(x,y_i,z)$ for y_i = 100 µm, located approximately in the center of the spheroid. The images reveal that confocal-line detection is able to improve visually perceived contrast well above the level of scanned Gaussian beams. However, in the case of Gaussian beam illumination, the signal for large penetration depth (right side) becomes very weak and the structure of the cell walls is hardly visible anymore. We quantitatively investigated the penetration depth by integrating the images shown in Figs. 7(b)-7(d), along the x-axis to obtain p_{avg} (Fig. 7(e)). This measurement quantifies the beam's on-axis power similar to the Q-Values computed from numerical data in Section 4. We could confirm the simulation results and found that sectioned Bessel beams perform better than Gaussian beams and equally well as conventional Bessel beams regarding penetration into a scattering medium.

To quantify the image contrast, we computed the ratio of high-frequency and low-frequency image information. Similar as in [17], each image $p_y(x,z)$ was Fourier transformed to $\tilde{p}(k_x,k_z) = FT\left[p(x,z)\right]$ and the resulting spatial frequency domain image was separated into high (HSF, where $k_r = (k_x^2 + k_z^2)^{1/2} \geq k_F$) and low (LSF, where $k_r < k_F$) contributions separated by the corner frequency k_F = 1.1/µm. The ratio of the integrated high- and low-frequency contributions

$$C = \frac{\mathrm{HSF}}{\mathrm{LSF}} = \frac{\iint_{k_r \geq k_F} \left|\tilde{p}(k_x,k_z)\right| dk_x dk_z}{\iint_{k_r < k_F} \left|\tilde{p}(k_x,k_z)\right| dk_x dk_z} \tag{14}$$

provides a quality parameter for image contrast C as previously in [7]. This expression is especially useful as it effectively describes the usable in-focus intensity signals (HSF) relative to the out-of-focus image intensity (LSF). Figure 9(f) shows the contrast $C(y_i)$ for all image planes $p(x,y_i,z)$. The measurement confirms the visual perception: confocal-line detection

#185263 - $15.00 USD Received 12 Feb 2013; revised 8 Apr 2013; accepted 12 Apr 2013; published 2 May 2013

increases image contrast for all illumination modes. The contrast $C(y_i)$ depends also on the plane y_i of the image inside the spheroid which is due to scattering of the fluorescence on the detection side. Figure 9(f) also reveals that sectioned Bessel beams offer better contrast than conventional Bessel beams. The values $C(y)$ are similar to Gaussian beam illumination. However by comparing Fig. 9(b) and 9(d) one can directly see that the sectioned Bessel beam yields a more favorable combination of overall image contrast and image detail at large penetration depths.

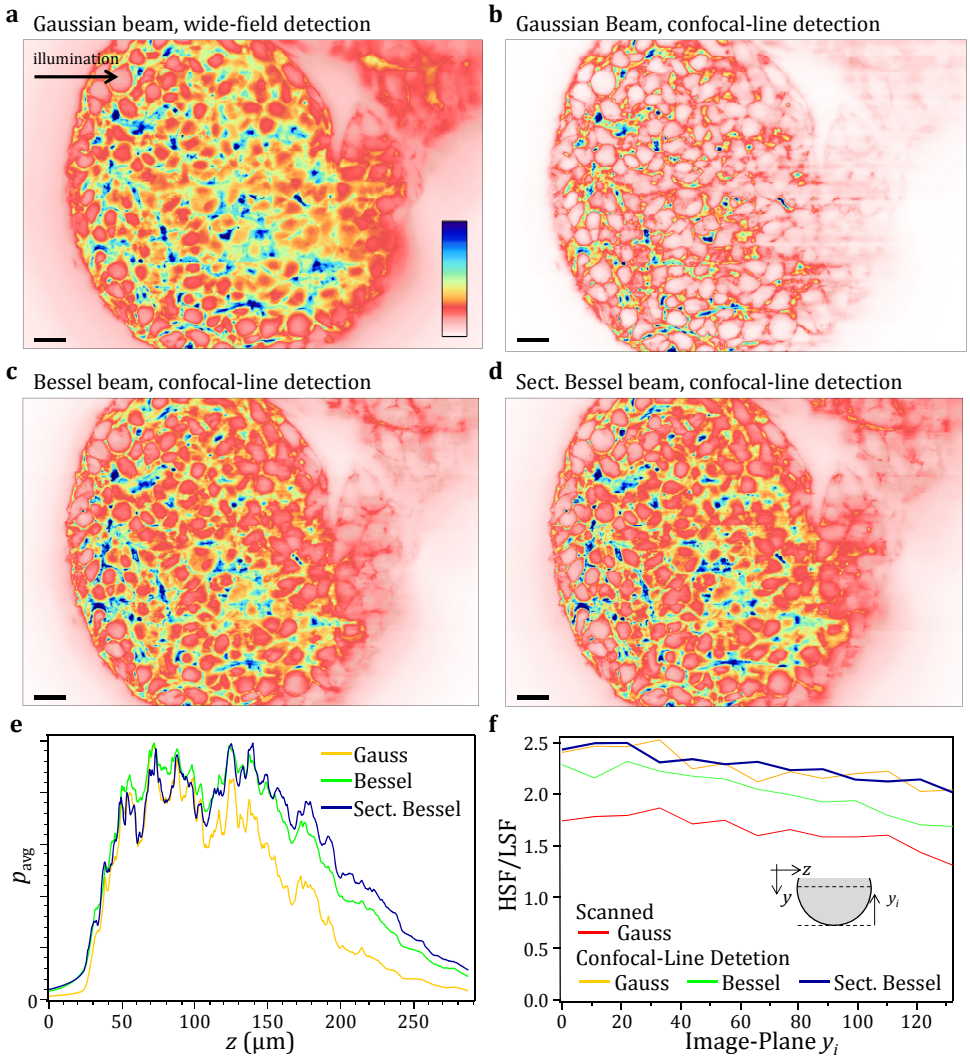

Fig. 9. Images of Tumor multicellular spheroids. Images of spheroidal cell clusters were imaged with Gaussian beam illumination using wide-field detection **(a)**, and using confocal-line detection **(b)** For Bessel beams **(c)** and sectioned Bessel beams **(d)** images are shown only with confocal line-detection. The size of the scalebar is 20µm. The illumination beams propagate from left to right. **(e)** The average image intensity along the propagation axis for b,c,d. **(f)** The image contrast measured by the ratio of and low spatial frequencies for the whole image stack. Layers deeper within the spheroid (larger i) show less contrast.

#185263 - $15.00 USD Received 12 Feb 2013; revised 8 Apr 2013; accepted 12 Apr 2013; published 2 May 2013

10. Discussion

The extents *dx*, *dy*, *dz* of a sectioned Bessel beam (SBB) in free space were described by evaluating the extents dk_x, dk_y, dk_z of its finite width ring spectrum in *k*-space, which is mainly defined by the sectioning angle β and the ring width parameter ε. These criteria give a good estimate for the dimensions of the illumination beams when scattering is negligible.

To be able to compare the performance of different beams in scattering media we calculated their directional propagation stability. By computing the beam power within a small area around the beam propagation axis *Q* we were able to directly quantify many important beam properties that are of great interest to microscopy: the penetration depth into inhomogeneous media and the influence of the position of the beam in the scattering medium on the beam shape. Beams that show superior directional propagation stability are beneficial to light-sheet microscopy in two ways: an increased penetration depth and reduced artifacts. In contrast to the self-similarity of the transverse beam profile [18] our measure allows a direct comparison to the experimental data acquired in a light-sheet microscope using the confocal-line detection mode.

Directional propagation stability was observed in simulation data of coherent beam propagation in scattering media consisting of spheres with two different sizes and densities (Figs. 3-5). Thereby, the random distributions of the spheres extended over the whole cross-section of the beams. The Bessel beam with the higher NA and therefore larger cross-section is significantly more robust to scattering. However, the similar performance of the conventional and the sectioned Bessel beam indicates that the self-reconstruction ability depends on the radial component of the wave-vectors. For β = 88°, the sectioned Bessel beam exhibits a cross section that is only half as large as that of the conventional Bessel beam. While the conventional Bessel beam is affected by more scatterers, the relative weight of each is smaller than in the case of the sectioned Bessel beam. Therefore, in a medium where the scatterers are homogeneously distributed, the average perturbation of the phase of the Bessel beam and the sectioned Bessel beam over their cross-sections are similar.

In the images of tumor multicellular spheroids, sectioned Bessel beams offer similar signal-to-background as Gaussian beams when combined with confocal-line detection. However, especially in the back of the sample, sectioned Bessel beams offer significantly higher signal strength. We measured an increase in contrast over conventional Bessel beams of approximately 15%. Based on the data obtained by simulations (Figs. 7 and 8), where the sectioned Bessel beam was found to provide 4 times better optical sectioning, one would expect an even larger increase in signal-to-background. There are two explanations for the moderate increase in measured signal-to-background. First, as can be seen in Fig. 6, the conventional Bessel beam provides the highest frequencies along the detection optical axis due to its highly confined central lobe. Therefore, even though the background is higher, the conventional Bessel beam is able to illuminate the sample in close proximity to the focal plane of the detection lens with a high intensity and provide high spatial-frequency image details. Several details in Fig. 9 show that Bessel beams are able to reveal very fine structures within the samples that are blurred by Gaussian beam illumination even though these beams provide better overall signal-to-background. Second, the image of the structure itself is not entirely composed of high-spatial frequency components. It is very likely that both the Gaussian beam (for low penetration depth) and the sectioned Bessel beam illuminate only a thin slice within the sample and yield an image that is composed of a comparable ratio of high to low spatial frequencies that is limited not by the illumination but by the fluorophore distribution and scattering on the detection side.

In dependence of the section angle β, we investigated the amount of the potential photo-damage produced by SBBs, by analyzing that fraction of the beam that illuminates fluorophores only along the confocal line as previously in [4, 7]. The ratio $\eta = P/E$ of the beam energy *P* within a circular region with radius *R* around the propagation axis *z* ($P(z;R)$

#185263 - $15.00 USD Received 12 Feb 2013; revised 8 Apr 2013; accepted 12 Apr 2013; published 2 May 2013

according to Eq. (4)) and the total beam energy $E = P(z,\infty)$, is a useful measure for the fraction of the beam's energy that excites fluorophores within the confocal volume. It is expected that this illumination efficiency η decreases for β<180°, especially for small values as for β = 20° (shown in Fig. 7(c)). However, within the range β>100° (Fig. 7(b)) that improves optical sectioning, the decrease in efficiency η in comparison to conventional Bessel beams (Fig. 7(a)) is small, especially for higher NAs and ring widths ε. For example, for NA = 0.4, ε = 0.8, the efficiency decreases by ≈30% for β = 100°, but for NA = 0.4 and ε = 0.9, the decrease of η for values of β>100° is only <10% in comparison to the conventional Bessel beam. These values were obtained from simulated data for R = 1μm. In conclusion, to maximize the efficiency η, the largest value of β that still enables good optical sectioning should be used. For example, as can be seen in Fig. 9, β = 140° already provides much better optical sectioning than the conventional Bessel beams for NA_{det} = 0.8. We expect that even higher values of β are suited for lower detection NAs that are often used for light-sheet microscopy of samples with a size of several hundred microns.

According to our simulations, the light efficiency η = P/E of a suitable SBB (large β) is slightly lower than that of a Bessel beam. However, the optical sectioning of a SBB is much better than that of a conventional BB. For example, for NA = 0.4 and ε = 0.9, one needs to increase the illumination intensity by 10% to gain a factor of 2 in sectioning (SBG) by using a SBB with β = 100°. This SGB value was computed according to Eq. (13) with $G(y)$ shown in Fig. 7(i) for a depth of field of the detection lens of 4μm.

SBBs in wide-field detection with scanned illumination beams [3, 5] offer much better optical sectioning than conventional Bessel beams according to our computer simulations. Because no fluorescence is rejected by the slit detection, the signal S is created by all fluorophores within a slice around the focal plane of the detection lens (with thickness corresponding to its depth of field). For this case, using numerical data, we computed an efficiency η, that is approx. 3-5 times higher than for confocal-line detection [7]. However, the optical sectioning is generally worse for wide-field detection (Fig. 7(j)) resulting in lower signal-to-background. Nevertheless SBBs with angles β = 30°…50°, where optical sectioning is best to, could be used illuminate large samples that are sensitive to light exposure. This allows to exploit the deeper penetration into strongly scattering media in comparison to Gaussian beams (Fig. 4).

11. Summary and conclusion

In summary, we have introduced a new variation of a Bessel beam, the sectioned Bessel beam. By simulating and measuring its performance in strongly scattering media we found that the directional propagation stability is equal to that of conventional Bessel beams.

To achieve the best optical sectioning, sectioned Bessel beams should be used in a confocal-line detection light-sheet microscope. According to our computer simulations, optical sectioning is 3 times better than for Gaussian beams already at a depth of field of 100μm and even larger for more extended samples that are typically imaged in light-sheet microscopy. Since optical sectioning of sectioned Bessel beams with confocal-line detection is independent of the field of view along the illumination axis, these beams enable submicron optical sections even in very large. These advantages make sectioned Bessel beams an ideal candidate for illuminating large samples in light-sheet microscopy.

Acknowledgments

We thank Cristian Gohn-Kreuz for helpful discussions. This work was financed by the Baden-Württemberg Stiftung.

#185263 - $15.00 USD Received 12 Feb 2013; revised 8 Apr 2013; accepted 12 Apr 2013; published 2 May 2013